This paper is published open source in *JGR: Oceans and can be accessed here:* https://doi.org/10.1029/2020JC016841.
Atkinson, J.; Esteves, L.S.; Williams, J.J.; Bell, P.S. and McCann, D.L., 2021. Nearshore Monitoring With X‐Band Radar: Maximizing Utility in Dynamic and Complex Environments. *JGR: Oceans,* 126(4), e2020JC016841.

Nearshore Monitoring with X-Band Radar: Maximising Utility in Dynamic and Complex Environments

J. Atkinson[1*], L. S. Esteves[1], J. J. Williams[2], P. S. Bell[3], and D. L. McCann[3]

[1] Faculty of Science & Technology, Bournemouth University, Poole, UK.

[2] Ports, Coastal & Offshore, Mott MacDonald Ltd, Croydon, UK.

[3] National Oceanography Centre, Liverpool, UK.

Corresponding author: Luciana S. Esteves (lesteves@bournemouth.ac.uk)

[*]Current affiliation: Ørsted UK, Howick Place, London, UK.

Key Points:

- Uncertainty in radar-derived bathymetry (2.5-10 m depths) was greatly reduced using a new data processing and quality control framework.
- Bathymetry changes were assessed for periods as short as 3 weeks were shown to be accurate to ±0.50 m at a 40x40 m resolution.
- The volume of nearshore sediment movement over a few weeks was comparable with annual longshore transport rates reported in this area.

Abstract

Coastal management and engineering applications require data that quantify the nature and magnitude of changes in nearshore bathymetry. However, bathymetric surveys are usually infrequent due to high costs and complex logistics. This study demonstrates that ground-based X-band radar offers a cost-effective means to monitor nearshore changes at relatively high frequency and over large areas. A new data quality and processing framework was developed to reduce uncertainties in the estimates of radar-derived bathymetry and tested using data from an 18-month installation at Thorpeness (UK). In addition to data calibration and validation, two new elements are integrated to reduce the influence of data scatter and outliers: (a) an automated selection of periods of 'good data' and (b) the application of a *depth-memory* stabilisation. For conditions when the wave height is >1 m, the accuracy of the radar-derived depths is shown to be ±0.5 m (95% confidence interval) at 40x40 m spatial resolution. At Thorpeness, radar-derived bathymetry changes exceeding this error were observed at timescales ranging from three weeks to six months. These data enabled quantification of changes in nearshore sediment volume at frequencies and spatial cover that would be difficult and/or expensive to obtain by other methods. It is shown that the volume of nearshore sediment movement occurring at timescale as short as few weeks are comparable with the annual longshore transport rates reported in this area. The use of radar can provide an early warning of changes in offshore bathymetry likely to impact vulnerable coastal locations.

Plain Language Summary

Near the shore, waves and currents can cause natural changes in seabed elevation (due to removal or deposition of mud, sand and gravel). On the other hand, changes in seabed elevation can alter the waves approaching the shore and influence the location and amount of coastal erosion. Measurements of these changes are required for coastal management and a wide range of engineering works. However, surveys of the seabed are usually infrequent owing to high costs and logistical difficulties. This paper analyses data from a marine radar installed on a cliff top to produce a series of seabed elevation (bathymetric) maps off the Thorpeness coast (UK). A new data quality assessment was developed to produce improved estimates of water depth. Results demonstrate that radar can offer a cost-effective alternative to conventional surveys and enable frequent monitoring of the seabed over large areas. The use of radar in the present study enabled the measurement of changes in nearshore seabed elevation within periods as short as three weeks. Radar-derived bathymetric maps can provide an early warning of seabed changes and allow more time to plan and implement responses to mitigate the impacts of coastal erosion.

1 Introduction

Being able to accurately and consistently monitor beach and nearshore processes provides the foundation for understanding beach dynamics (Davidson et al., 2007). The control on waves by changing nearshore bathymetry has been the subject of increased research interest, primarily to understand and predict shoreline changes (Hequette et al., 2009; Hequette and Aernouts, 2010; Lazarus & Murray, 2011; Ruessink et al., 2004; Stokes et al., 2015). Nearshore sediment accretion provides protection to the coast during the first high energy events that follow periods of low energy (Dissanayake et al., 2015). Conversely, coastal erosion hotspots have been attributed to the concentration of wave energy caused by complex nearshore geology (Browder and McNinch, 2006; Burningham and French, 2017; Schupp et al., 2006; Williams et al., 2019). These processes are controlled further by changes in the incident wave climate (Hegermiller et al., 2017; Lazarus & Murray, 2011), particularly wave direction bimodality (Burningham and French, 2016, 2017; Williams et al., 2019).

Quantifying magnitudes of coastal change and understanding drivers of temporal and spatial variability is required to inform coastal management decisions (Atkinson & Esteves, 2018; Pye & Blott, 2006; Smit et al., 2007). Coastal researchers and managers increasingly need to employ a range of techniques to conceptualise site-specific morphodynamic behaviour. Although technology advances enabled more accurate monitoring of beach changes and over large areas (Burvingt et al., 2017), challenges persist regarding quantifying bathymetric changes in the nearshore (Kotilainen & Kaskela, 2017; Pacheco et al., 2015).

Direct measurements of nearshore waves, hydrodynamics and the seabed require expensive *in situ* installations of sensors that have limited spatial coverage (e.g. current meters and wave buoys) and deployment from vessels (e.g. multibeam surveys), which have limitations in shallow waters (Costa et al., 2009). Remote sensing methods are often constrained by the sensors' ability to 'see' at times of unfavourable weather or water conditions during storms or high energy events, exactly when largest nearshore changes are expected to occur. Bathymetric Light Detection and Ranging (LiDAR) and satellite sensors can be used in areas of minimal water turbidity but show large errors where water transparency is low and in areas of breaking waves (Chust et al., 2010; Costa et al., 2009; Kotilainen & Kaskela, 2017). While results obtained from multispectral Dove satellites imagery show vertical root-mean-square error between 1.22 and 1.86 m for depths of 4 to 10 m at 4 m spatial resolution based on best cloud-free and minimal turbidity conditions (Li et al., 2019), the temporal resolution and accuracy of satellite imagery remain limited by cloud cover.

Video systems, such as Argus (Aarnikhof & Holman, 1999; Holman et al., 1993; Holman & Stanley, 2007; Kroon et al., 2007; Smit et al., 2007) have been used to: derive water depths and basic wave and current parameters (Holman et al., 2013); monitor changes in shoreline position (Kroon et al., 2007); and understand surf zone bar dynamics (Masselink et al., 2014) and intertidal changes (Davidson et al., 2007; Smit et al., 2007). The use of video systems is restricted by daylight hours and weather-related visibility and requires image rectification and geometric corrections if cameras move due to wind or other factors. Further, these systems have a limited field of view (maximum 1000-1500 m per camera) and pixel resolution increases with distance, exceeding 40 m at 1500 m from the camera (Holman and Stanley 2007). Radar offers the benefits of being able to record data irrespective of daylight, under a wide range of weather and visibility conditions (except heavy rainfall, calm winds and low waves), it does not require image correction and generally has a larger field of view. Information of bathymetry, waves and surface currents have been extracted from X-band radar images of the sea surface over 4-5 km radius (Bell et al., 2011; McCann & Bell, 2014; Bell et al., 2016).

X-band radar as a remote sensing tool relies on the presence of backscatter known as 'sea clutter', generated by a combination of direct reflections (sea spikes) and Bragg scattering from small capillary ripples on the sea surface and further modulated by sea surface waves (Skolnik, 1980). Through a frequency domain analysis (e.g. Fourier transform) the spectral characteristics of ocean surface waves can be inferred from the sea clutter, and from these, wave parameters such as frequency and wavelength can be calculated. Hydrographic properties can also be inferred using the physics of dispersive waves through the 'wave inversion' method, which is well-established with X-band radar (Bell, 1999; Hessner and Bell, 2009; Ludeno et al., 2015, Lund et al., 2020). Most recently, cBathy (Holman et al., 2013) has been applied to derive nearshore bathymetry from both camera images and radar data (Honegger et al., 2019; Honegger et al., 2020; Gawehn et al., 2020). So far, the application of radar-derived bathymetry to understand nearshore change has been limited to research applications due to the complexity involved in assessing data quality.

This paper presents a new framework of data processing and quality assessment applied to data obtained from an 18-month radar deployment at Thorpeness (Suffolk) on the east coast of the UK. Previous work (Atkinson et al., 2018) showed that ~90% of water depths derived from these radar data were within ±1m of the depths measured by concurrent multibeam surveys and ~60% of data were within ±0.5m. Results presented here advance the previous work by showing that the application of this new framework has considerably improved this accuracy; warranting the production of radar-derived bathymetric maps from which sediment volume changes in dynamic nearshore areas can be estimated for periods as short as three weeks. To facilitate the application of the framework to data obtained elsewhere and by other systems, the approaches incorporated into the framework are described in more detail in the Supplementary Information.

2 Study Site

The radar system was installed on a clifftop at the north end of Thorpeness village (52.182°N, 1.613°E, Suffolk, East England), a dynamic mixed sand and gravel coast showing a prominent cuspate gravel foreland (locally called the ness) to the north (Figure 1). The beach morphology shows high temporal and spatial variability and is influenced by underwater geology, bimodal wave direction and coastal protection works (Atkinson and Esteves, 2018). The nearshore is characterised by mobile banks, and complex underlying hard geology showing 2-km wide underwater ridges extending 12 km SW-NE offshore from the coast. These ridges are formed by cemented fine sands and silts of the Pliocene Coralline Crag formation (Long and Zalasiewicz, 2011). A dynamic nearshore seabed feature south of the ness has been shown to respond to the bimodal wave direction (Atkinson et al., 2018). Modelling simulations indicate the feature contributes in part to the occurrence of episodic erosion hotspots along the Thorpeness village frontage (Williams et al., 2019). Similar effects of nearshore banks were observed elsewhere along the Suffolk coast (Burningham & French, 2016).

The site is exposed to a semi-diurnal mesotidal regime with peak astronomical range ~2.5 m and storm surges that can exceed 2 m, with water levels reaching 3.78 m above Ordnance Datum Newlyn, ODN (Wadey et al., 2015). Offshore waves show bimodal direction, with the peak direction (DirP) oscillating between southwest and northeast (based on the Cefas WaveNet West Gabbard buoy, 51.952°N 002.109°E, 41 m depth) year to year and within the years, without reflecting a strong seasonal signal (Atkinson and Esteves, 2018).

3 Methods

This section describes the new data processing and quality assessment framework used to analyse the X-band radar data collected between 16-Sep-2015 and 18-Apr-2017 (Atkinson et al., 2020). The workflow of the individual steps involved in the framework is shown in Figure 2. For brevity and to improve readability, this section focuses on the new data quality assessment (DQA) steps and the selection of 'good data' (H_s threshold filter). Further details of the methods are provided in the Supporting Information.

3.1 The radar system

The radar system comprised a Kelvin Hughes 10 kW, 9.41 GHz marine X-band radar system with a 2.4 m horizontally polarised antenna has a 3 dB horizontal beamwidth of ~0.8 degrees and a mean rotation time of ~2.6 seconds. The radar was set to transmit 60ns pulses of radar energy at 3000 pulses per second. The radar transceiver and antenna were installed on a 12-m high scaffold tower on a clifftop overlooking the study area, at a total elevation of ~20 m above mean sea level (Figure 1). The data analysis focused on an area of 3.3 km^2 of the radar view (1.5 km alongshore x 2.2 km offshore).

The radar was set up to record 256 rotations of the antenna, (2.63 seconds per rotation) in approximately 11-minute data bursts every 30 minutes; generating a time-series 'image stack' each time. The radar was connected to the commercially available WaMoS II analogue-to-digital converter developed by OceanWaveS GmbH, which digitised the radar video signal in raw 'B-scan' polar coordinate format at 32 MHz, corresponding to a range resolution of 4.68m. The WaMoS II wave processing software was used to derive wave spectral parameters from the radar data immediately after each record was digitised, yielding an estimated (uncalibrated) significant wave height (H_s), peak wave period (T_p), mean wave period (T_m), mean wave direction (DirM) and peak mean direction (DirP). WaMoS II uses algorithms well-documented in the literature to measure sea state conditions from X-band radar data (Hessner et al., 2014, 2015; Reichert et al., 1999; Wyatt et al., 2003).

Following digitisation and derivation of 'raw' wave parameters, each raw 'B-scan' polar-coordinate radar image stack was then pre-processed automatically on-site to remove non-uniformities in the antenna rotation rate due to wind effects. The resulting data were then resampled to produce a final uniform angular resolution of three pulses per degree to reduce the files sizes stored on an internal hard drive. The compressed polar files were downloaded during site visits and, off-site, they were converted from polar to cartesian coordinates on a 5m grid (OSGB36) via bi-linear interpolation. The processing described in this paragraph is represented in the workflow (Figure 2) as 'NOC' functions (as they were undertaken using scripts written by the authors affiliated at the NOC). The wave inversion method was then applied to generate bathymetric maps (Section 3.2).

3.2 Estimating water depth

This section describes the data processing and quality control involved in the estimation of water depth from radar data, including the size of the analysis window, which defines the resolution of the bathymetric maps, and the new *depth memory* stabilisation, a decaying average procedure to improve the estimation of water depth. Water depths were estimated using the bathymetric inversion algorithms based on the linear wave theory (Borge et al. 2004; Bell, 1999; Bell & Osler, 2011):

$$\boldsymbol{\omega} = \sqrt{\boldsymbol{gk}\,\mathbf{tanh}(\boldsymbol{kh})} + \boldsymbol{u}\cdot\boldsymbol{k} \quad (1)$$

where ω is angular wave frequency, g is the acceleration due to gravity, k is the wavenumber, h is the mean water depth, and u is the surface current velocity. Many approaches have been proposed to derive the wave parameters from radar data (see Chernyshov et al., 2020). Here, the wave parameters were calculated using a 3D Fast Fourier Transform (FFT) over a finite water surface area (i.e. the 'analysis window'). The analysis window must be large enough to cover at least one wavelength in all directions and homogeneity is assumed of both k and the frequency spectra. Crucially, the wave inversion method can only function with enough wavelengths within the analysis window. Therefore, selecting the size of the analysis window is important (see Section 3.2.1 and Supporting Information S1).

For simplicity, underlying currents are often assumed to have minimal effect on wave propagation (Bell, 1999; Bell & Osler, 2011; Honegger et al., 2019). At the study site, tidally-induced currents exceed 1.5 m s^{-1} (Lees, 1983) and waves often approach the coast at an oblique angle, implying the potential for significant wave-current interaction. The near-surface currents were obtained by calculating the Doppler shift for each wavenumber within each analysis window, given a water depth value. Incorporating the depth and current analysis within each analysis window provides an 'instantaneous' estimation of the water depth as a non-gaussian probability density function (PDF) for each image stack. The peak of the PDF describes the 'most probable depth' at a point centred in the analysis window.

The iteration for each analysis box is obtained using proprietary NOC algorithms, in a manner similar to that of Senet et al. (2001). The results usually converge on the best estimates for each parameter given the observed wave signatures in each analysis box for each individual record. Due to the non-gaussian nature of the PDF, instantaneous measurements are generally noisy and are likely to introduce a bias to the final result. An average of sequential PDFs for a given analysis window can be taken to mitigate this bias and determine a more representative 'most probable depth'. The calculation also needs to allow the seabed to evolve over time, which is achieved through (a) a windowing function or (b) by allowing each PDF to decay in importance with time in the manner of a radioactive half-life. The latter technique (hereafter the *depth- memory*) is used in this framework (see Section 3.2.2). The *depth-memory* has been developed initially for operational near-real-time use of X-band radar as a practical monitoring tool, a medium to long-term goal of the authors.

3.2.1 The analysis window size

In effect, the 3D-FFT approach counts the number of waves in a given analysis window, split by observed frequency. FFTs only distinguish integer numbers of waves in each dimension. The higher the numbers of waves within the analysis window, the better the wavelength resolution. As the wave energy spreads across adjacent bins, the ability to accurately measure wavelengths decreases when the size of the analysis window is small relative to the wavelength of the waveforms. The closer the wavelength is to the size of the analysis box, the worse this 'spectral leakage' effect becomes. The method limits the spatial resolution of the resulting bathymetric maps by requiring that each side of the analysis window be at least 100-200 m depending on wave characteristics (Honegger et al., 2019). To mitigate the low wavenumber issue, the 3D-FFT was augmented using a Phase-Locked Loop type algorithm to precisely identify the dominant 2D wavelength signal at each wave frequency (Bell & Osler, 2011).

The size of the analysis window also influences the dimensions of the morphological features that can be resolved. Only features of the same order of magnitude or larger than the analysis window can be resolved. There is no 'one size fits all' solution regarding the size of the analysis window, as this depends on local wave conditions and the needs of specific applications. Larger analysis windows include more wave data, generally producing less noisy results due to greater spatial averaging. This, in turn, is likely to violate the assumption of homogeneity. Considering the characteristics of local waves with 90% of observed wave periods < 8s and maximum water depths in the nearshore under 13m (Figure S1), an analysis window of 160x160 m was used in this study. The reasoning underpinning this selection is explained in the Supporting Information S1.

To create a spatial map of calculated hydrographic parameters, the analysis window is stepped spatially with the parameters calculated for the centre of the box. After optimisation against water depths measured by multibeam surveys (described in Atkinson et al., 2018), bathymetry was derived by shifting the 160x160 m analysis window in 40 m increments throughout the radar field-of-view (Figure 3). The window size acts inherently as a low pass filter on the detected bathymetry. This process resulted in a 40x40 m bathymetry grid that enabled seabed changes and features of interest to be resolved.

The sampling theorem might suggest that a 50% overlap between successive box positions in a given dimension would be the optimum translation interval to capture the variations in water depths detectable by this method. Based on the authors' experience in the analysis of radar data, this spacing is shown to be too coarse. The translation of a quarter of the analysis window size yields a significantly smoother result without excessive oversampling, and this has been adopted here. Other methods could be used to estimate the wavenumber-frequency pairs on an almost pixel-by-pixel basis using cross-spectral analysis. However, they show the same signal-to-noise limitations as the FFT-based spectral methods and, under normal operational conditions, would require an equivalent amount of spatial averaging to overcome this. Wavelet analysis can also be applied, but the level of smoothing required was shown to have limited ability to resolve variable bathymetry (Chernysov et al., 2020).

3.2.2 *Depth-memory* stabilisation

In the *depth-memory* approach, an integration *half-life time* is defined in terms of the number of records (R_n). When the approach is first initialised at a new site, each new probability function for a given geographic location is corrected for the tide level. This ensures that depths are relative to the chosen datum. The records are then added together until the defined consecutive R_n value is reached. If R_n is set to 10, record 1 makes up 1/10 (0.1) of the total PDF after the tenth record is reached. In this case, records 1 to 10 are defined as the *depth-memory* stabilisation period so that:

- After 11 records, record 1 makes up (1/10)*(1-1/10) = 0.090 of the total;
- After 12 records, record 1 makes up 0.09*(1-1/10) = 0.081 of the total; and
- After 13 records, record 1 makes up 0.081*(1-1/10) = 0.073 of the total and so on.

After ~20 records, the influence of record 1 to the integrated PDF has halved to 1/20. By records 32 and 54, it has decayed to less than 1/100 and 1/1000, respectively. The selected value for R_n is highly dependent on the activity of the seabed. At sites where the seabed is immobile, a large R_n value can be defined and a long term, stable bathymetric map can be derived. At sites where the seabed is dynamic and complex, a shorter R_n value is required to prevent previous records dominating the average and a change ’lag’ occurring (i.e. the depth memory is continually catching up with the present state).

When defining the *depth-memory* R_n the interplay between the processing resolution and wave climate needs to be established. The effect of wave climate is shown from two starting points selected within 72 hours of each other (Figure 4): Scenario 1 (09-Oct-2019 0000 to 1130) occurred during low waves (H_s<1 m) with variable peak direction (DirP) indicative of a low energy sea; and Scenario 2 (11-Oct- 2015 1200 to 2330) occurred during moderate wave heights (H_s = 1.25 to 1.8 m) with a sustained northerly DirP. Figure 4 shows the derived bathymetric maps after 1, 6 and 24 records (30 minutes, 3 and 12 hours respectively) for Scenario 1 (top row, 1a-c) and 2 (bottom row 2a-c). Although distinct bathymetric features emerge in both cases, after 24 records of low wave height (Scenario 1), the shape of the nearshore seabed is less well defined than after 6 records of wave heights exceeding 1 m (Scenario 2).

Although the scenarios above focus on the differences in wave height, the detectability of waves in sea clutter is affected by the angle between the radar antenna look and peak wave direction (Lund et al. 2014) and depends on the combination of wind speed and wave height. This wind speed and wave height interplay is particularly important in relatively fetch-limited coasts where locally-generated waves dominate, such as in the area of Thorpeness. The radar ability to register the sea surface is impaired under low wind (<3 m/s) and wave conditions (0.5-1 m significant wave height). During periods of low sea clutter, the data processing algorithms struggled to define wave parameters and to obtain an accurate wave inversion. Consequently, there is greater uncertainty in depth estimations under Scenario 1 conditions, and longer R_n values are required to produce a stable bathymetric map. However, seabed changes more often occur under high wave conditions; therefore, there is generally more need and interest in measuring changes caused by these conditions.

3.3 Selecting ‘good data’

Low wave and wind conditions impose limitations on radar-derived data that can greatly increase the uncertainty of water depth estimates and the resulting bathymetric maps. To ensure consistency in data quality, bathymetric maps were created only for periods (defined by R_n) of ‘good data’. In the absence of wind data and considering that wave heights < 1 m result in low rates of bedload sediment transport and small bathymetric changes, ‘good data’ was identified through an H_s threshold filter and a ‘stable memory finder’ (Figure 2). H_s > 1 m was the simplest and most influential variable and threshold to identify blocks of ‘good data’ to produce bathymetric maps. Combining other variables as part of the filter would add complexity to the automated data quality control but may improve the selection of ‘good data’. The H_s filter was applied on calibrated radar-derived data after the *depth-memory* length and quality control procedures described above were performed. The selection of ‘good data’ involved the following steps:

a) The filter was used to identify all records showing calibrated H_s > 1 m;

b) The ‘stable memory finder’ screened the filtered records to identify all periods in which H_s > 1 m for at least 12 hours (24 records).

c) The screening identified the first *data block* in which the *depth memory* had stabilised (i.e. depths within the PDF were calculated from data exceeding the wave height threshold in the previous 12 hours).

d) If H_s dropped below the threshold, the *data block* was closed, and a new *data block* initiated when data met the criteria. Bathymetric maps were then produced for each *data block* fitting the criteria.

During the radar deployment period, 53 *data blocks* were identified using this filtering method. The longest gap between *data blocks* was 80 days (between 06-Mar-2016 and 25-May-2016). Using a bespoke graphical user interface developed in Matlab, bathymetric changes within each *data block* were analysed to identify outliers informed by known magnitudes of change obtained from multibeam surveys. Changes that were too large or in areas expected to be immobile were filtered out of the analysis. The water depth variance was then assessed to remove artefacts related to changes in water level, variations in wave direction and nonlinearities in the wave climate across radar field-of-view. The bathymetric maps derived from radar data passing the quality control screening were then analysed to: (a) quantify the magnitude and location of significant bathymetric changes, and (b) identify the driving metocean conditions. This step identified areas where significant seabed changes were expected, and calculations of sediment volume changes were then performed only for these areas.

3.4 Tidal correction

To relate radar-derived depth to a datum and to allow averaging over consecutive records, the algorithms require tidal elevation data that include astronomical and meteorological forcing. This can be provided from a tide gauge or through a ‘synthetic’ tide approach, in which a meteorological (residual) value from a nearby tide gauge can be added to the harmonic prediction at the site (e.g. Bell et al., 2016).

In this study, a synthetic tide approach was validated against data from a pressure sensor deployed for 3 months (27-Apr-2016 to 31-Jul-2016) within a drainage sluice located 2 km south of Thorpeness. The pressure sensor was installed approximately at mean sea level (the lowest possible elevation due to site limitations); thus, only water levels above this elevation could be recorded (see Figure 5). These data allowed calibration of observed water levels against (a) a synthetic tide derived from residuals from a permanent Class 1 tide gauge at Lowestoft (45 km north of Thorpeness); and (b) POLPRED harmonic prediction (NOC, 2019) close to the radar deployment site. A good agreement was obtained between the measured and synthetic tidal time-series; except during a storm surge (14-15 May 2016) when the model underestimated the observed water levels (Figure 5a). This illustrates well the need to include the meteorological component (tidal residual) in the synthetic tide. Adding the Lowestoft tidal residual values to the astronomical predictions improved the correlation coefficient R^2 from 0.75 (Figure 5b) to 0.96 (Figure 5c).

For this study, the synthetic tide (comprising the predicted and meteorological components of the tide) was subtracted from the water levels derived from each radar record to reference those depths to chart datum, thus allowing the estimated depths to be integrated over time relative to a static vertical reference (i.e. chart datum). To achieve this in an (ideal) situation with near-real-time processing, the system would need to receive a real-time water level measurement from a (local) tide gauge. A tidal prediction could be substituted in the absence of suitable tide gauge data, but the absence of the meteorological component would inevitably introduce errors. Accounting for the meteorological component is very important, since the radar typically delivers the best quality wave imagery when waves are high, and these are often associated with a positive surge.

3.5 Wave height calibration

Due to the nonlinearity of the radar imaging mechanism, wave height cannot be inferred directly from the raw data (Borge et al., 1999). However, a calibration can be applied to the radar data using coincident wave measurements from another instrument (Alpers & Hasselmann, 1982). Here, time-series of significant wave height (H_s) from the Cefas wave buoy located ~1900 m north and ~3500 m east of the radar were used to calibrate the radar-derived wave height (Figure 5d) using the relationship:

$$H_s = A + B\sqrt{SNR} \qquad (2)$$

where A is the intercept and B the slope of the fit between the Signal-to-Noise Ratio of the dispersion relation fit (SNR, calculated by the WaMoS II software). The resulting calibrated H_s relationship was used subsequently in the radar data quality control process (Figure 2) as described in Section 3.2.2. A strong correlation (R^2=0.74) was found between calibrated radar-derived H_s and the wave measurements (Figure 5d). Some uncertainty remains in the estimates of wave heights and thus in the accuracy of the H_s threshold filter. Although some of the selected 'good data' might not have an actual H_s >1 m, the filter offers a simple means to identify data with reasonable wave signal. It is important to note that Figure 5d shows good agreement for H_s <2m reassuring that the radar-derived estimates are suitable to identify the low wave periods that will be excluded from the analysis.

3.6 Validation of radar-derived bathymetry

Validation of radar-derived bathymetry was undertaken using concurrent multibeam surveys conducted in January 2017 (during a period of wave heights ~1.5 m) resampled to 40x40m, the same spatial resolution as the radar wave inversion (Atkinson et al., 2018). The multibeam surveys conducted at the time of the radar installation were commissioned by the Maritime Coastguard Authority and were independent of this research. Using the data quality control framework described here, the validation was redone and compared with the results of Atkinson et al. (2018) to assess the improvements that can be achieved. Results of this validation are presented in Section 4 and improvements discussed in Section 5.

4 Results

Following the quality control assessment, a comparison between calibrated radar-derived and measured bathymetry showed that 96% of radar-derived values were within ±0.5 m of the measured data and 100% within ±1 m (Figure 6a). A very strong linear correlation (R^2=0.98, 95% confidence interval) between radar-derived depths and multibeam survey measurements was obtained even for uncalibrated data (Figure 6b). Results indicate a slight deviation from the line of equivalence whereby shallower depths tend to be overestimated, and deeper depths are underestimated, similar to results reported by Rutten et al. (2017). Comparing radar-derived bathymetry (Figure 6c) with the concurrent multibeam survey show an underestimation of radar-derived depths along the beach foreshore south of the radar and an overestimation in an area north of the radar extending south and offshore from the ness (Figure 6d). The multibeam data are the only available ‘ground truth’ for the radar-derived bathymetry shown here; however, they are not a perfect measure of the seabed. For example, Figure 7a shows evidence of vessel track lines within the data, suggesting imperfect correction for vessel motion. These data are referenced vertically using kinematic GPS and thus translation to chart datum is independent of the water level at the vessel. In contrast, the radar-derived depth is corrected to chart datum through a synthetic tidal elevation (Section 3.3), which is assumed flat across the study area at a point in time corresponding to the middle of the radar image sequence.

Differences between the radar-derived depth and multibeam data may result from several factors, and it is not possible to isolate which may be the greatest contributor:

(a) Nonlinearities in wave behaviour due to increasing wave steepness and breaking increase as water depth decreases. This will manifest as waves travelling slightly faster than linear wave theory might predict and hence lead to an overestimation of depth in shallower water.

(b) The discontinuity of the rapidly shallowing seabed and shoreline representing the worst-case scenario for an FFT based analysis that assumes homogeneity within the analysis window.

(c) The predominance of locally generated short wavelength, short period waves becoming less sensitive to water depth in deeper areas of the study areas. Figure S1 demonstrates that only waves of approximately 6 seconds and above would feel the seabed adequately to fulfil either criteria of 90% or 95% of deep-water behaviour down to the 13m maximum water depth expected in the study area.

(d) The predominance of short period, short wavelength waves may have an adverse impact on the determination of currents. The effective depth of a current corresponding to a given wavelength moves towards the surface as the wavelength of the waves decreases (Campana et al., 2016, 2017; Lund et al, 2020). At a certain point, the wind-driven surface current will disproportionately start to manifest in the Doppler shift (used to infer the current) of the shortest waves that have a very near surface effective depth, affecting the calculated water depth.

Despite the factors described above, Figure 6d shows conclusively that the differences are partially attributable to actual seabed changes measured between the multibeam survey periods. The multibeam bathymetry was produced by surveys undertaken over four weeks in January 2017 when relatively high energy events occurred. The radar-derived bathymetry was produced with ‘good data’ obtained on 13-Jan-2017 when waves approached from N.E. with H_s>1.5 m and peak period of 10 s.

4.1 Identifying areas of nearshore change

Knowing where seabed changes are expected, and the magnitude of changes, can help scrutinise radar data. Comparing the bathymetry recorded by two multibeam surveys undertaken in July 2014 (Figure 7a) and January 2017 (Figure 7b)), it was possible to identify areas of mobile and immobile seabed (Figure 7c). Except for areas closest to shore and across the central sector of the radar view (indicated by the black outline in Figure 7 c,d) where largest changes are evident, the seabed is mostly immobile (i.e. changes are within ±0.125 m the error band of the data). Bands of erosion aligned approximately north-south across the survey area (Figure 7c) are artefacts of the 2014 survey data (Figure 7a), as they align with the trajectory of the vessel. Figure 7d represents the bathymetric changes shown in Figure 7c resampled to the spatial resolution (40x40m) of the radar-derived depth, and the depth values accounted for the estimated radar uncertainty. This allows identification of three areas (numbered 1, 2, 3) where seabed changes and their probable magnitudes could be expected to be measured by radar data.

Area 1 shows erosion (up to -2 m) of an oblique bar extending off the ness evident in the 2014 survey. In Area 2, accretion occurs (up to +2 m) just south of Area 1. There is an abrupt transition between erosion in Area 1 and accretion in Area 2. Area 3 shows erosion (up to -1.5 m) in the surf zone along most of the southern half of the survey area, including the beach frontage of Thorpeness village. The large changes observed offshore of Area 2 (Figure 7c) are reduced to just a few pixels in Figure 7d and, therefore, are likely too narrow to be adequately resolved by the radar at the spatial resolution of the wave inversion analysis. These narrow bands of erosion and accretion suggest a north-westerly migration of large (c. 2 m high, 20-50 m wide) bedforms.

4.2 Quantifying nearshore changes

To illustrate the radar-derived bathymetry produced in this study and the ability to measure changes at a range of time-frames, examples are provided here of longer-term (4-6 months, Figure 8) and short-term (3-9 weeks, Figure 9) changes. This analysis only considered changes exceeding 0.5 m. Changes observed in Areas 1, 2 and 3 for selected periods of 4 to 6 months (Figure 8e-g) and 3 to 9 weeks (Figure 9e-g) are used to estimate changes in sediment volumes (Table 1).

Analysis of the radar-derived bathymetry show marked changes over 4 to 6 months, particularly in Areas 1 and 2 (Figure 8, Table 1), commensurate with the differences observed between the two multibeam surveys (Figure 7d). At these timescales, accretion in Area 1 seems to occur alongside erosion of Area 2 (Figure 8e) and *vice-versa* (Figure 8 f,g). From 11-Oct-2015 to 06-Feb-2016, depths increased in Areas 2 and 3 (Figure 8e) resulting in an estimated sediment volume loss of 26,063 m^3 and 11,653 m^3, respectively (Table 1). During the same period, sediment accretion in Area 1 amounted to 112,196 m^3 (Table 1), with maximum changes in seabed elevation reaching +1.75 m. Between 06-Feb-2016 and 20-Aug-2016, magnitudes of change were considerably lower, and the pattern of change reversed in Areas 1 and 2, with erosion continuing in Area 3 (Table 1). Area 1 lost 36,453 m^3 of sediment volume (a maximum bathymetric change of -1.15 m), and Area 2 gained 16,818 m^3 (a maximum vertical change of +0.89 m). Changes intensified from 20-Aug-2016 to 23-Feb-2017, with erosion continuing in Area 1 (-71,343 m^3) and accretion in Area 2 (+35,241 m^3), with no changes in Area 3.

Short-term analysis of sediment volume changes focused on three consecutive periods spanning from October 2015 to February 2016 (Figure 9, Table 1). The two first periods provide insights into the changes occurring within the longer-term period 11-Oct-2015 to 06-Feb-2016 analysed previously. From 11-Oct-2015 to 10-Dec-2015, accretion occurred in Area 1 (+44,588 m^3), with erosion dominating in Area 2 (a net loss of -5,272 m^3). In the subsequent period (10-Dec-2015 and 06-Feb-2016), changes continued and intensified, with larger volume gain (in less time) occurring in Area 1, greater sediment loss in Area 2 (-8,763 m^3) and erosion (-10,635 m^3) also extending into Area 3 (Figure 9f). In the following three weeks, there was a switch in the pattern of changes, Area 1 experienced net erosion and Area 2 accretion, with magnitudes of volume gain (31,116 m^3) similar to the changes estimated over five months from Aug 2016 to Feb 2017 (Table 1).

The losses and gains in sediment volume presented in Table 1 are conservative and exclude all areas where changes are within the error of radar-derived bathymetry. Over shorter periods, magnitudes of bathymetric change are often small, except for some areas. Consequently, more areas are excluded from the analysis when compared with analyses over longer periods. The short-term analyses, therefore, can underestimate the volume changes. This is apparent when comparing the changes in Area 1 for the period 11-Oct-2015 to 06-Feb-2016 (112,196 m^3) with the sum of the changes in the two shorter-periods (a total of 98,083 m^3) that cover the same time (Table 1). There is a difference of 14,113 m^3 or 12.5 % of the volume. Similarly, a difference of 42% was found between the shorter-term (14,904 m^3) and the longer-term (26,083 m^3) estimated erosion volume in Area 2.

5 Discussion

The framework for data quality assessment applied here, includes water level and wave height calibration, ground-truth of radar-derived bathymetry with simultaneous multibeam surveys, and a rigorous selection of data based on optimum site-specific wave conditions. This new framework has enabled an improved quantification of uncertainties associated with radar-derived bathymetric data and resulted in enhanced accuracy of results. The application of this framework in the validation of radar-derived bathymetry using multibeam survey data showed results much improved than the ones reported by Atkinson et al. (2018). These authors reported uncertainty of ±1 m for ~90% of radar-derived depths and ±0.5 m for ~60% of grid cells with linear regression correlation coefficient R^2= 0.93. In the present study, 96% of radar-derived values were within ±0.5 m of the measured data and 100% within ±1 m with a stronger linear correlation (R^2=0.98, 95% confidence interval) (Figure 6). The improved accuracy enabled, for the first time, insight into the rates and patterns of sediment volume changes in the nearshore at time-frames from a few weeks to a few months were obtained from radar data.

In accord with work from less complex coastal environments (e.g. Hessner and Bell, 2009; Ludeno et al., 2015), the present work has shown that the accuracy of radar-derived bathymetric obtained during ideal conditions is ±0.5 m in depths down to 10m. This figure is in line with the higher end of the 5-10% accuracy range quoted by Piotrowski & Dugan (2002) for data originating from an optical system onboard a military drone and using similar mathematical techniques. This accuracy is equivalent to depths extracted from video-systems (Holman et al., 2013) and considerably better than reported from bathymetric lidar (Chust et al., 2010); and satellite data (Li et al., 2019; Traganos et al., 2018). In contrast to Rutten et al. (2017) who showed the greatest accuracy was achieved in water depths greater than 6 m below MSL, this study showed the highest accuracy in shallower waters between 2 to -8 m ODN, with the deeper regions within the radar field-of-view showing significant inaccuracies. It is considered that these differences are attributable to the size of the analysis window (160x160 m in this study and 960x960 m in Rutten et al. (2017).

When compared with other ground-based remote sensing techniques, the radar shows greater limitations on the spatial resolution and advantages concerning the range of conditions it can be operational. X-band radar can capture good quality data under most weather conditions, independently of water transparency (a limitation of bathymetric lidar) and daylight (limitations of video-systems). Further, its range extends beyond that of most shore-based camera systems. Both the video-systems (Holman et al., 1991) and the radar (Bell et al., 2016) enable bathymetric mapping in the intertidal zone using a waterline tracing method. However, the relatively small tidal range and the steepness of the mixed sand-gravel beach at the study site were not conducive to the application of this technique.

The evidence presented here shows that radar can be used as a nearshore monitoring tool for general trends in erosion or accretion and define the sediment volume changes in specified areas at a temporal resolution spanning weeks or months. This evidence contrasts with Rutten et al. (2017) conclusions which argued that due to substantial bias in shallower regions and to the resolution of the radar, daily to monthly volume changes estimated from radar data are unrealistic. The present accurate nearshore volume change estimates have been made possible in the present study by the analysis framework employed, which focusses on the nearshore region with higher resolution at the cost of data quality loss in deeper water.

In order to put the scale of the observed sediment volume changes into context it is useful to note that the volume change figures for regions 1 and 2 in particular listed in Table 1 for each event are of a similar order of magnitude to the estimated annual longshore sediment transport budget of that part of the coast (Vincent, 1979; Royal Haskoning, 2009). Given that the movement of such large scale sediment features will be dependent on the directional balance, intensity and sequencing of wave events in any given year, it is now intuitively easy to understand how that section of coastline at Thorpeness may be prone to fluctuations in erosion and deposition, which was the underlying reason for deploying the radar system for this project.

6 Conclusions

Using multibeam survey validation data, and robust quality control and data analysis procedures, bathymetric maps have been derived from X-band radar data acquired during an 18-month installation at Thorpeness, UK. This paper shows that the accuracy of the radar-derived nearshore bathymetry can be improved through the application of a new framework of data processing and quality assessment described here. Two new elements are included in this framework, a *depth memory* stabilisation and a filter to select ‘good data’. Using this analysis framework, the radar-derived bathymetry is shown to be accurate to ±0.50 m down to 10 m water depth at a 40x40 m resolution, and changes exceeding this error were measured in time-spans of weeks. The results obtained in this study would not have been possible using traditional survey methods without an extensive and expensive field monitoring campaign.

Radar-derived bathymetry enabled observation of two distinct nearshore morphology states in which seabed features formed and subsequently eroded on timescales between 4 and 12 months. Quantification of bathymetric changes and estimated sediment volumes were possible for periods as short as three weeks. These data show that, in dynamic areas within the radar view, changes within a few weeks can have magnitudes similar to the observed within 4-6 months. The results demonstrate, therefore, the viability of X-Band radar as a cost-effective tool for monitoring nearshore changes in bathymetry along dynamic coasts.

Acknowledgments and Data Availability

This work was conducted as part of John Atkinson’s PhD project, co-funded by Bournemouth University, Mott MacDonald and Suffolk Coastal District Council. Radar data used in this research were obtained through the project “X-band radar and evidence-based coastal management decisions” funded by the UK. Natural Environment Research Council Innovation grant (NE/M021653/1 and NE/M021564/1). The authors would like to thank: Paul Patterson from Coastal Partnership East for his extensive cooperation and support in arranging and dealing with radar installation requirements; Mr Glen Ogilvy for his kind permission for the temporary installation of the radar on his land; Gary Watson at the Environment Agency for facilitating the temporary installation of the pressure sensor in the Thorpeness Sluice; and the support and contribution from Thorpeness residents, particularly: Fred Monson, Mike Chandler, Lucy Ansbro and Mr/Mrs Moore. The authors declare no real or perceived financial conflicts of interests.

All data used in the production of this paper (Atkinson et al., 2020) has been banked with the British Oceanographic Data Centre and is available from https://www.bodc.ac.uk/data (short doi:10/fdff).

References

Aarninkhof, S.G.J., & Holman, R.A. (1999), Monitoring the nearshore with video. *Backscatter*, 10(2), 8-11.

Alpers, W.R., & Hasselmann, K. (1982), Spectral signal to clutter and thermal noise properties of ocean wave imaging synthetic aperture radars. *Journal of Remote Sensing,* 3, 423–446. doi.org/10.1080/01431168208948413.

Atkinson, J., & Esteves, L.S. (2018), Alongshore variability in the response of a mixed sand and gravel beach to bimodal wave direction. *Geosciences*, 8. doi.org/10.3390/geosciences8120488

Atkinson J.; Esteves L.S.; Williams J.J.; Bell P.S.; & McCann D.L. (2020), X-band radar derived wave parameters and depth maps in the area of Thorpeness, Suffolk, UK between August 2015 and March 2017. British Oceanographic Data Centre, National Oceanography Centre, NERC, UK, doi:10.5285/b0b0a132-092b-7c3b-e053-6c86abc08a9e.

Atkinson, J., Esteves, L.S., Williams, J.W., & McCann, D.L., Bell, P.S. (2018), The Application of X-Band Radar for Characterization of Nearshore Dynamics on a Mixed Sand and Gravel Beach. *Journal of Coastal Research, SI*85, 281–285. doi.org/10.2112/si85-057.1.

Bell, P.S. (1999), Shallow water bathymetry derived from an analysis of X-band marine radar images of waves. *Coastal Enginering,* 37, 513–527. doi.org/10.1016/S0378-3839(99)00041-1.

Bell, P.S., Bird, C.O., & Plater, A.J. (2016), A temporal waterline approach to mapping intertidal areas using X-band marine radar. *Coastal Enginering*, 107, 84–101. doi.org/10.1016/j.coastaleng.2015.09.009

Bell, P.S., & Osler, J.C. (2011), Mapping bathymetry using X-band marine radar data recorded from a moving vessel. *Ocean Dynamics*, 61, 2141–2156. doi.org/10.1007/s10236-011-0478-4

Bell, P.S., Williams, J.J., Clark, S., Morris, B.D., & Vila-Concejo, A. (2004), Nested Radar Systems for Remote Coastal Observations. *Journal of Coastal Research,* SI39, 483–487.

Borge, J.C.N., Hessner, K., & Reichert, K. (1999), Estimation of the Significant Wave Height With X-Band Nautical Radars. *Proc. 18th International Conference Offshore Mech* 1–8.

Borge, J.C.N.; Rodriguez, G.R.; Hessner, K. & Gonzalez, P.I. (2004), Inversion of Marine Radar Images for Surface Wave Analysis. *Journal of Atmospheric and Oceanic Technology*, 21, 1291-1300.

Brooks, S.M., & Spencer, T. (2012), Shoreline retreat and sediment release in response to accelerating sea level rise: Measuring and modelling cliffline dynamics on the Suffolk Coast, U.K. *Global and Planetary Change*, 80–81, 165–179. doi.org/10.1016/j.gloplacha.2011.10.008

Brooks, S.M., & Spencer, T. (2010), Temporal and spatial variations in recession rates and sediment release from soft rock cliffs, Suffolk coast, U.K. *Geomorpholog,y* 124, 26–41. doi.org/10.1016/j.geomorph.2010.08.005

Browder, A.G., & McNinch, J.E. (2006), Linking framework geology and nearshore morphology: Correlation of paleo-channels with shore-oblique sandbars and gravel outcrops. *Marine Geol*ogy, 231, 141–162. doi.org/10.1016/j.margeo.2006.06.006.

Burningham, H. & French, J. (2017), Understanding coastal change using shoreline trend analysis supported by cluster-based segmentation. *Geomorphology,* 282, 131–149. doi.org/10.1016/j.geomorph.2016.12.029

Burningham, H., & French, J. (2016), Shoreline-Shoreface Dynamics on the Suffolk Coast. CERU Report No. 1608-1, The Crown Estate (2016), ISBN 978-1-906410-76-6, 117 p.

Burvingt, O., Masselink, G., Russell, P., Scott, T.M. (2017), Classification of beach response to extreme storms. *Geomorphology* 295, 722–737. doi.org/10.1016/j.geomorph.2017.07.022.

Campana, J., Terrill, E. J., & de Paolo, T. (2016), The development of an inversion technique to extract vertical current profiles from X-band radar observations. *Journal of Atmospheric and Oceanic Technology,* 33(9), 2015-2028.

Campana, J., Terrill, E. J., & de Paolo, T. (2017). A new inversion method to obtain upper-ocean current-depth profiles using X-band observations of deep water waves. *Journal of Atmospheric and Oceanic Technology*, 34 (5), 957-970.

Chernyshov, P., Vrecica, T., Streßer, M., Carrasco, R., & Toledo, Y. (2020), Rapid wavelet-based bathymetry inversion method for nearshore X-band radars. *Remote Sensing of Environment*, 240, 111688. doi.org/10.1016/j.rse.2020.111688.

Chust, G., Grande, M., Galparsoro, I., Uriarte, A., & Borja, A. (2010), Capabilities of the bathymetric Hawk Eye LiDAR for coastal habitat mapping: A case study within a Basque estuary. Estuarine, *Coastal and Shelf Science*, 89(3), 200-213. doi.org/10.1016/j.ecss.2010.07.002.

Costa, B.M.; Battista, T.A. & Pittman, S.J., (2009). Comparative evaluation of airborne LiDAR and ship-based multibeam SoNAR bathymetry and intensity for mapping coral reef ecosystems. *Remote Sensing of Environment*, 113(5), 1082-1100. doi.org/10.1016/j.rse.2009.01.015.

Davidson, M.A., Van Koningsveld, M., de Kruif, A., Rawson, J., Holman, R.A., Lamberti, A., Medina, R., Kroon, A., & Aarninkhof, S. (2007), The CoastView project: Developing video-derived Coastal State Indicators in support of coastal zone management. *Coastal Engineering*, 54, 463–475. doi.org/10.1016/j.coastaleng.2007.01.007.

Davidson-Arnott, R.G.D., & Greenwood, B. (2003), Waves and sediment transport in the nearshore zone. *Coastal Zones and Estuaries*, 43–60.

Deng, A., & Stauffer, D. R. (2006), On improving 4-km mesoscale model simulations. *Journal of Applied Meteorology and Climatology*, *45*(3), 361–381. doi:10.1175/JAM2341.1.

Digimap (2004). Hydroview Reference [WWW Document].

Dissanayake, P., Brown, J., Wisse, & P., Karunarathna, H. (2015), Effects of storm clustering on beach/dune evolution. *Marine Geology,* 370, 63–75. doi.org/10.1016/j.margeo.2015.10.010.

Gawehn, M., van Dongeren, A., de Vries, S., Swinkels, C., Hoekstra, R., Aarninkhof, S., & Friedman, J. (2020), The application of a radar-based depth inversion method to monitor nearshore nourishments on an open sandy coast and an ebb-tidal delta. *Coastal Engineering,* 159, doi.org/10.1016/j.coastaleng.2020.103716.

Hegermiller, C.A., Rueda, A., Erikson, L.H., Barnard, P.L., Antolinez, J.A.A., & Mendez, F.J. (2017), Controls of Multimodal Wave Conditions in a Complex Coastal Setting. *Geophysical Research Letters,* 44, 12,315-12,323. doi.org/10.1002/2017GL075272.

Hequette, A., & Aernouts, D. (2010), The influence of nearshore sand bank dynamics on shoreline evolution in a macrotidal coastal environment, Calais, northern France. *Continental Shelf Research*, 30, 1349-1361. doi.org/10.1016/j.csr.2010.04.017.

Hequette, A., Ruz, M.H., Maspataud, A., & Sipka, V. (2009), Effects Of Nearshore Sand Bank And Associated Channel On Beach Hydrodynamics: Implications For Beach And Shoreline Evolution. *Journal of Coastal Research*, SI56, 59–63.

Hessner, K., & Bell, P.S. (2009), High resolution current & bathymetry determined by nautical X-Band radar in shallow waters. *OCEANS 2009-EUROPE,* 1–5. doi.org/10.1109/OCEANSE.2009.5278333

Hessner, K., Reichert, K., Borge, J.C.N., Stevens, C.L., & Smith, M.J. (2014), High-resolution X-Band radar measurements of currents, bathymetry and sea state in highly inhomogeneous coastal areas. *Ocean Dynamics,* 64, 989-998. doi.org/10.1007/s10236-014-0724-7

Hessner, K., Wallbridge, S., & Dolphin, T. (2015), Validation of areal wave and current measurements based on X-band radar. *Currents, Waves and Turbulence Measurement* 2015, 1-10. doi.org/10.1109/CWTM.2015.7098102

Holman, R.A.; Sallenger, J.A.H.; Lippmann, T.C., & Haines J.W. (1993), The application of video image processing to the study of nearshore processes. *Oceanography,* 6(3), 78-85. doi.org/10.5670/oceanog.1993.02

Holman, R.A., Plant, N., & Holland, T. (2013), CBathy: A robust algorithm for estimating nearshore bathymetry. *JGR Oceans,* 118, 2595–2609. doi.org/10.1002/jgrc.20199.

Holman, R.A., & Stanley, J. (2007), The history and technical capabilities of Argus. *Coastal Engineering*, 54, 477–491. doi.org/10.1016/j.coastaleng.2007.01.003

Honegger, D.A., Haller, M.C., & Holman, R.A. (2019), High-resolution bathymetry estimates via X-band marine radar: 1. beaches. *Coastal Engineering,* 149, 39-48. doi.org/10.1016/j.coastaleng.2019.03.003.

Honegger, D.A., Haller, M.C., & Holman, R.A. (2020), High-resolution bathymetry estimates via X-band marine radar: 2. Effects of currents at tidal inlets. *Coastal Engineering,* 156, doi.org/10.1016/j.coastaleng.2019.103626

Koilainen, A.T., & Kaskela, A.M. (2017), Comparison of airborne LiDAR and shipboard acoustic data in complex shallow water environments: Filling in the white ribbon zone. *Marine Geology*, 385, 250-259. doi.org/10.1016/j.margeo.2017.02.005.

Kroon, A.; Davidson, M.A.; Aarninkhof, S.G.J.; Archetti, R.; Armaroli, C.; Gonzalez, M.; Medri, S.; Osorio, A.; Aagaard, T.; Holman, R.A. & Spanhoff, R. (2007), Application of remote sensing video systems to coastline management problems. *Coastal Engineering*, 54(6-7), 493-505. doi.org/10.1016/j.coastaleng.2007.01.004

Lazarus, E.D., & Murray, A.B. (2011), An integrated hypothesis for regional patterns of shoreline change along the Northern North Carolina Outer Banks, USA. *Marine Geology*, 281, 85-90. doi.org/10.1016/j.margeo.2011.02.002.

Lee, E.M. (2008), Coastal cliff behaviour: Observations on the relationship between beach levels and recession rates. *Geomorphology*, 101, 558–571. doi.org/10.1016/j.geomorph.2008.02.010.

Lees, B.J. (1983), Sizewell-Dunwich Banks field study topic report: 7. Final report. A study of nearshore sediment transport processes. Wormley, UK, Institute of Oceanographic Sciences Report 146, 45pp.

Li, J.; Knapp, D.E.; Schill, S.R.; Roelfsema, C.; Phinn, S.; Silman, M.; Mascaro, J., & Asner, G.P. (2019), Adaptive bathymetry estimation for shallow coastal waters using Planet Dove satellites. *Remote Sensing of Environment*, 232, 111302. doi.org/10.1016/j.rse.2019.111302.

Long, P.E., & Zalasiewicz, J.A. (2011), The molluscan fauna of the Coralline Crag (Pliocene, Zanclean) at Raydon Hall, Suffolk, UK: Palaeoecological significance reassessed. *Palaeogeography, Palaeoclimatology, Palaeoecology*, 309, 53–72. doi.org/10.1016/j.palaeo.2011.05.039

Lopez, G., Conley, D.C., & Greaves, D. (2016), Calibration, Validation, and Analysis of an Empirical Algorithm for the Retrieval of Wave Spectra from H.F. Radar Sea Echo. *Journal of Atmospheric and Oceanic Technology*, 33, 245–261. doi.org/10.1175/JTECH-D-15-0159.1.

Ludeno, G., Reale, F., Dentale, F., Carratelli, E.P., Natale, A., Soldovieri, F., Serafino, F. (2015), An X-band radar system for bathymetry and wave field analysis in a harbour area. *Sensors*, 15, 1691–1707. doi.org/10.3390/s150101691.

Lund, B., Collins, C.O., Graber, H.C., Terrill, E., & Herbers, T.H.C. (2014), Marine radar ocean wave retrieval’s dependency on range and azimuth. *Ocean Dynamics* 64, 999-101. doi.org/10.1007/s10236-014-0725-6.

Lund, B., Haus, B.K., Graber, H.C., Horstmann, J., Carrasco, R., Novelli, G., Guigand, C.M., Mehta, S., Laxague, N.J.M., & Özgökmen, T.M. (2020), Marine X-band radar currents and bathymetry: An argument for a wave number-dependent retrieval method. *JGR Oceans* 125, doi.org/10.1029/2019JC015618.

Masselink, G., Austin, M., Scott, T.M., Poate, T., & Russell, P. (2014), Role of wave forcing, storms and NAO in outer bar dynamics on a high-energy, macro-tidal beach. *Geomorphology* 226, 76–93. doi.org/10.1016/j.geomorph.2014.07.025

McCann, D.L. & Bell, P.S. (2014), Marine radar derived current vector mapping at a planned commercial tidal stream turbine array in the Pentland Firth, U.K. 2014 *Oceans* - St. John's, doi.org/10.1109/OCEANS.2014.7003186

NOC (2019). POLPRED Technical Information. Retrieved 09-Mar-2021 https://noc-innovations.co.uk/sites/noc-innovations/files/documents/Info_PPW_technical_info.pdf

Pacheco, A.; Horta, J.; Loureiro, C. & Ferreira, O. (2015), Retrieval of nearshore bathymetry from Landsat 8 images: A tool for coastal monitoring in shallow waters. *Remote Sensing of Environment*, 159, 102-116. doi.org/10.1016/j.rse.2014.12.004.

Piotrowski, C.C. & Dugan, J.C. (2002), Accuracy of bathymetry and current retrievals from airborne optical time-series imaging of shoaling waves. *IEEE Transactions on Geoscience and Remote Sensing*, 40(12), 2606-2618. doi.org/10.1109/TGRS.2002.807578.

Pye, K., & Blott, S.J. (2006), Coastal Processes and Morphological Change in the Dunwich-Sizewell Area, Suffolk, U.K. *Journal of Coastal Research,* 223, 453–473. doi.org/10.2112/05-0603.1

Reichert, K., Hessner, K., Borge, J.C.N., & Dittmer, J. (1999), WaMoS II: A radar based wave and current monitoring system. Isope ’99 Proc. Vol. 3 3, 1–5.Royal Haskoning, 2009.Suffolk SMP2 Sub-cell 3c Review of coastal processes and Geomorphology. Draft Report. Suffolk Coastal District Council. Report RCP1/301164/PBor.

Ruessink, B.G., Van Enckevort, I.M.J., & Kuriyama, Y. (2004), Non-linear principal component analysis of nearshore bathymetry. *Marine Geology,* 203, 185–197. doi.org/10.1016/S0025-3227(03)00334-7.

Rutten, J., de Jong, S.M., & Ruessink, G. (2017), Accuracy of Nearshore Bathymetry Inverted From X-Band Radar and Optical Video Data. *IEEE Transactions on Geoscience and Remote Sensing*, 55, 1106–1116. doi.org/10.1109/TGRS.2016.2619481.

Schupp, C.A., McNinch, J.E., & List, J.H. (2006), Nearshore shore-oblique bars, gravel outcrops, and their correlation to shoreline change. *Marine Geology,* 233, 63–79. doi.org/10.1016/j.margeo.2006.08.007

Skolnik, M.L. (1980), Introduction to radar systems. ISBN 0-07-Y66572-9

Senet, C.M., Seemann, J., & Ziemer, F. (2001), The near-surface current velocity determined from image sequences of the sea surface. *IEEE Transactions on Geoscience and Remote Sensing,* 39(3), 492–505. doi.org/10.1109/36.911108

Sibson, R. (1981), Interpolating Multivariate Data. John Wiley, Chichester.

Smit, M.W.J., Aarninkhof, S.G.J., Wijnberg, K.M., Gonzlez, M., Kingston, K.S., Southgate, H.N., Ruessink, B.G., Holman, R.A., Siegle, E., Davidson, M.A., & Medina, R. (2007), The role of video imagery in predicting daily to monthly coastal evolution. *Coastal Engineering*, 54, 539–553. doi.org/10.1016/j.coastaleng.2007.01.009

Stewart, R.H. and Joy, J.W. (1974), H.F. radio measurement of surface currents. *Deep-Sea Research,* 21, 1039-1049. doi.org/10.1016/0011-7471(74)90066-7.

Stokes, C., Davidson, M.A., & Russell, P. (2015), Observation and prediction of three-dimensional morphology at a high-energy macrotidal beach. *Geomorphology* 243, 1–13. doi.org/10.1016/j.geomorph.2015.04.024

Traganos, D.; Poursanidis, D.; Aggarwal, B.; Chrysoulakis, N. & Reinartz, P. (2018), Estimating Satellite-Derived Bathymetry (SDB) with the Google Earth Engine and Sentinel-2. *Remote Sensing*, 10(6), 859. doi.org/10.3390/rs10060859.

Vincent, C.E. (1979), Longshore sand transport rates–a simple model for the East Anglian coastline. *Coastal Engineering*, 3, 113–136.

Wadey, M.P., Haigh, I.D., Nicholls, R.J., Brown, J.M., Horsburgh, K., Carroll, B., Gallop, S.L., Mason, T., & Bradshaw, E. (2015), A comparison of the 31 January–1 February 1953 and 5–6 December 2013 coastal flood events around the U.K. *Frontiers Marine Science*, 2. doi.org/10.3389/fmars.2015.00084.

Williams, J.J. (2014), Thorpeness Coastal Erosion Appraisal (347287/MMN/PCO/001/B 09), Mott MacDonald.

Williams, J.J.; Atkinson, J.; Price, D.M.; Esteves, L.S. & Costa, S.S. (2019), New understanding of a coastal erosion hotspot in a bimodel wave climate. *Coastal Sediments* '19, 817-829. doi: 10.1142/9789811204487_0072.

Wyatt, L.R., Green, J.J., Gurgel, K.W., Borge, J.C.N., Reichert, K., Hessner, K., Günther, H., Rosenthal, W., Saetra, O., & Reistad, M. (2003), Validation and intercomparisons of wave measurements and models during the EuroROSE experiments. *Coastal Engineering*, 48, 1–28. doi.org/10.1016/S0378-3839(02)00157-6.

Captions of Figures

Figure 1. Aerial view of the X-band radar installation site at the north end of the Thorpeness village, Suffolk (UK).

Figure 2. Flow diagram of the data processing and quality control framework employed to produce the radar-derived data.

Figure 3. An example of the 160x160 m analysis window (yellow) and the 40m step length (green) used in wave-inversion calculations to infer the water depth overlaid on a raw backscatter image showing waves approaching from the southeast.

Figure 4. Time-series (top panel) of significant wave height (H_s) and peak wave direction (DirP) identifying two 12-hour periods used to demonstrate the effects of the depth memory for low (Scenario 1) and moderate (Scenario 2) wave conditions on derived bathymetric maps at (a) record 1, instantaneous map, (b) record 6, 3 hours, and (c) record 24, 12 hours. Radar position is indicated by a red star. Land above MW is masked in black. Note that the visible artefact (~104º from north) was caused by a mechanical issue explained in Supporting Information S2.

Figure 5. (a) Synthetic water levels (incorporating tidal residuals at Lowestoft), POLPRED model predictions and observed water level recorded within the sluice over a three-day window (b) RMS analysis of POLPRED model and (c) synthetic water levels against observed water levels (>0 m only to reflect recorded data). (d) Calibrated radar-derived wave height against Sizewell directional Waverider data.

Figure 6. (a) Difference between multibeam measured water depths and radar-derived depths before (red line) and after (blue histogram) water level calibration with the synthetic tide. (b) Scatter plot of the depths obtained from multibeam surveys and from radar data (uncalibrated) showing the linear regression equation. (c) Radar-derived bathymetry concurrent to the multibeam survey. (d) Differences between multibeam and radar-derived depths, where negative values indicate underestimation of the radar data and positive values are an overestimation.

Figure 7. Bathymetry (1 m grid resolution) from two multibeam surveys covering the study area obtained (a) by the Environment Agency in June 2014 and (b) by the Maritime Coastal Authority in January 2017. (c) Differences between the two bathymetric maps, where negative values indicate an increase in depth and positive values indicate a reduction in depth (changes within the error band of the method ±0.125 m are blanked). (d) Resampling of map (c) to the same spatial resolution of the radar-derived depth and excluding changes within the error of the radar. The black line boundary in c,d indicates the area within the radar view used in the analysis. Thorpeness beach frontage buildings are identified in all figures.

Figure 8. Radar-derived bathymetry of the study area for (a) 11-Oct-2015, (b) 06-Feb-2016, (c) 20-Aug-2016, and (d) 23-Feb-2017 and (e, f, g) maps showing areas of large bathymetric differences (>0.5 m) between these dates. The numbered areas in (e) identify the three areas of largest changes. The red circle indicates radar position. The mean water line is shown as a black line.

Figure 9. Radar-derived bathymetry of the study area for (a) 11-Oct-2015, (b), 10-Dec-2015, (c) 06-Feb-2016, and (d) 28-Feb-2016 and (e, f, g) maps showing areas of large bathymetricifferences (>0.5 m) between these dates. The red circle indicates the radar position. The mean water line is shown as a black line.

Table 1. Areas where bathymetric changes exceed radar accuracy (±0.5 m) and respective estimated changes in sediment volume during longer and shorter periods within the three nearshore areas of interest.

Period		Nearshore change	Area 1		Area 2		Area 3	
			Area [m^2]	Volume [m^3]	Area [m^2]	Volume [m^3]	Area [m^2]	Volume [m^3]
Longer-term changes (4-6 months)								
11-Oct-2015	06-Feb-2016	Accretion	118,400	+112,196				
		Erosion			36,800	-26,063	19,200	-11,653
06-Feb-2016	20-Aug-2016	Accretion			25,600	+16,818		
		Erosion	48,000	-36,453			1,600	-1,068
20-Aug-2016	23-Feb-2017	Accretion			46,400	+35,241		
		Erosion	92,800	-71,343				
Shorter-term changes (3-9 weeks)								
11-Oct-2015	10-Dec-2015	Accretion	72,000	+44,588	1,600	+869		
		Erosion			9,600	-6,141		
10-Dec-2015	06-Feb-2016	Accretion	67,200	+53,495				
		Erosion			16,000	-8,763	17,600	-10,635
06-Feb-2016	28-Feb-2016	Accretion	6,400	+3,410	41,600	+31,116	1,600	+884
		Erosion	16,000	-9,382				

Figure 1.


UK
Thorpeness
N
Sizewell nuclear power station
Gravel cuspate foreland (the ness)
North end of Thorpeness village
2013 geobags
1970s gabions
13 Apr 2016, Photo by permission of www.mike-page.co.uk
Radar installation

Figure 2.

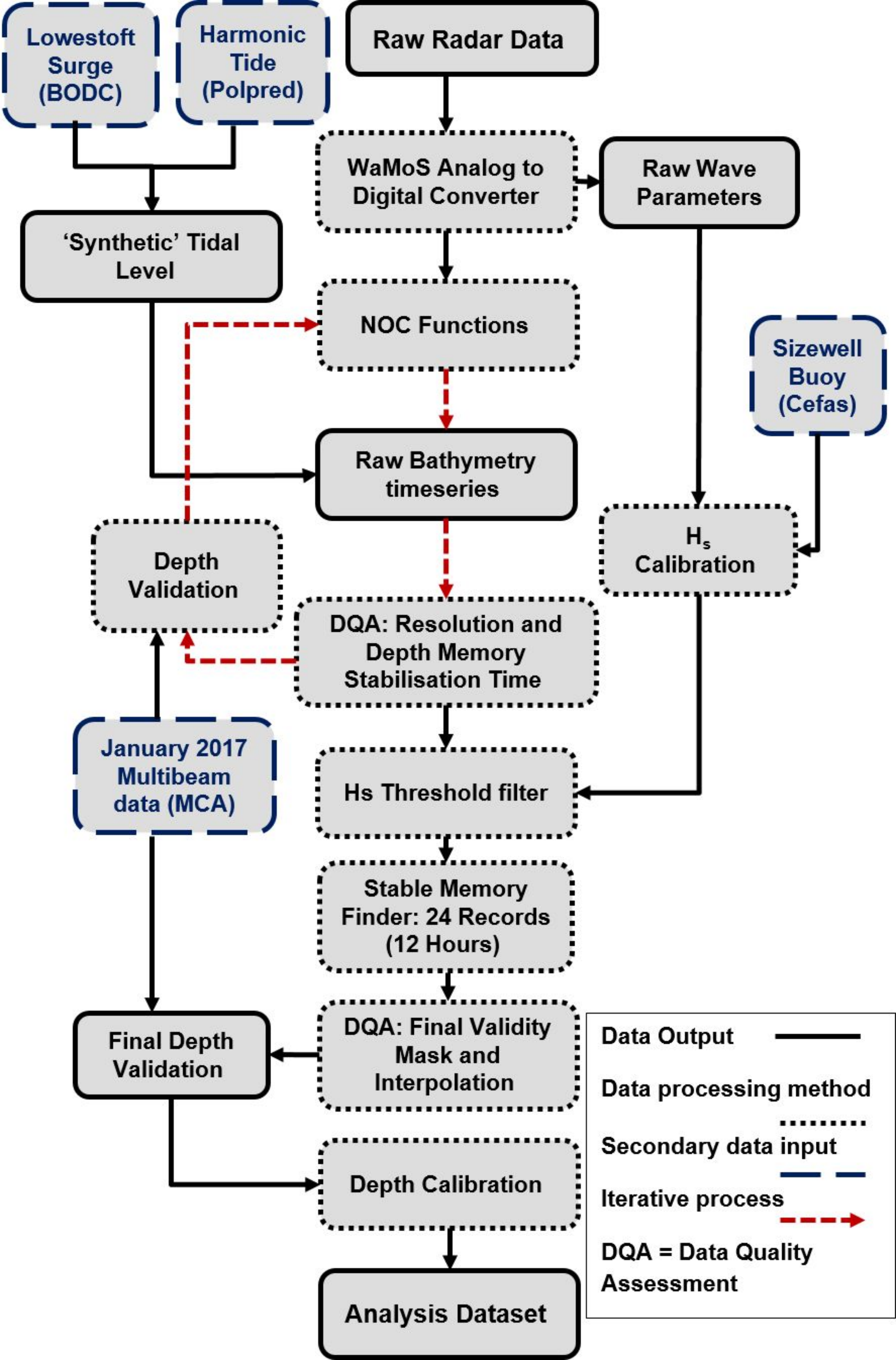
Lowestoft Surge (BODC)
Harmonic Tide (Polpred)
Raw Radar Data
WaMoS Analog to Digital Converter
Raw Wave Parameters
'Synthetic' Tidal Level
NOC Functions
Sizewell Buoy (Cefas)
Raw Bathymetry timeseries
Depth Validation
H_s Calibration
DQA: Resolution and Depth Memory Stabilisation Time
January 2017 Multibeam data (MCA)
Hs Threshold filter
Stable Memory Finder: 24 Records (12 Hours)
Final Depth Validation
DQA: Final Validity Mask and Interpolation
Depth Calibration
Analysis Dataset
Data Output
Data processing method
Secondary data input
Iterative process
DQA = Data Quality Assessment

Figure 3.

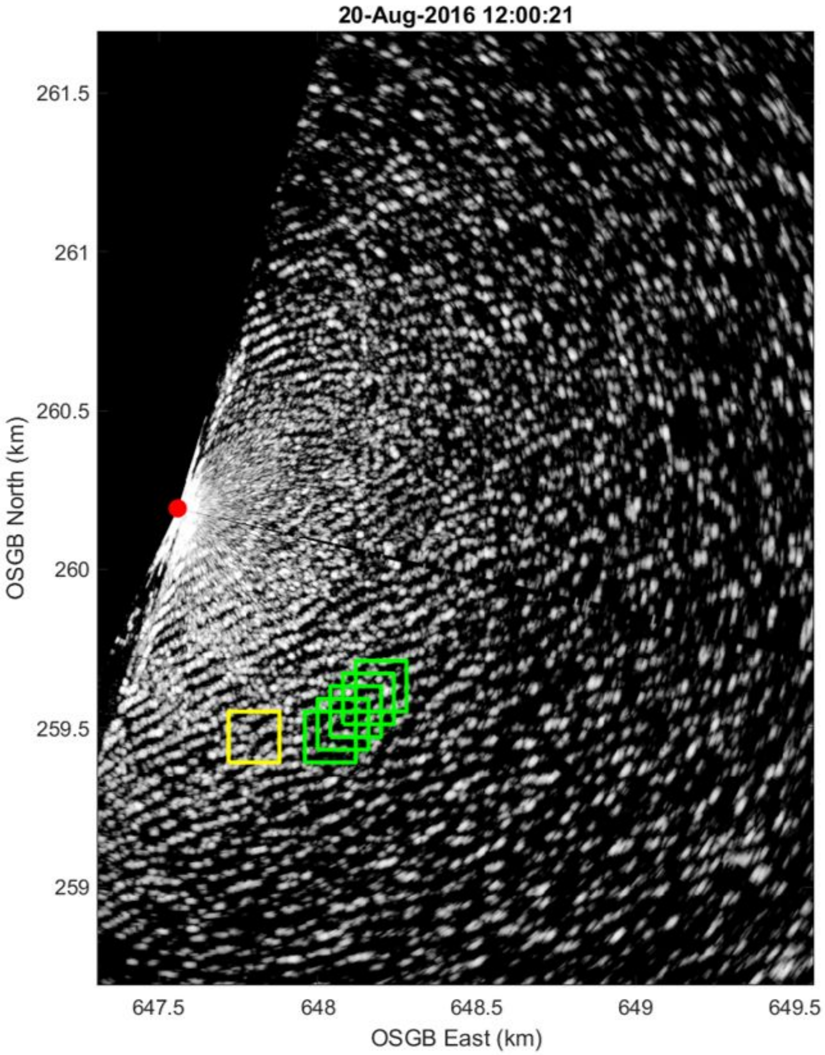
20-Aug-2016 12:00:21
261.5
261
260.5
260
259.5
259
OSGB North (km)
647.5
648
648.5
649
649.5
OSGB East (km)

Figure 4.

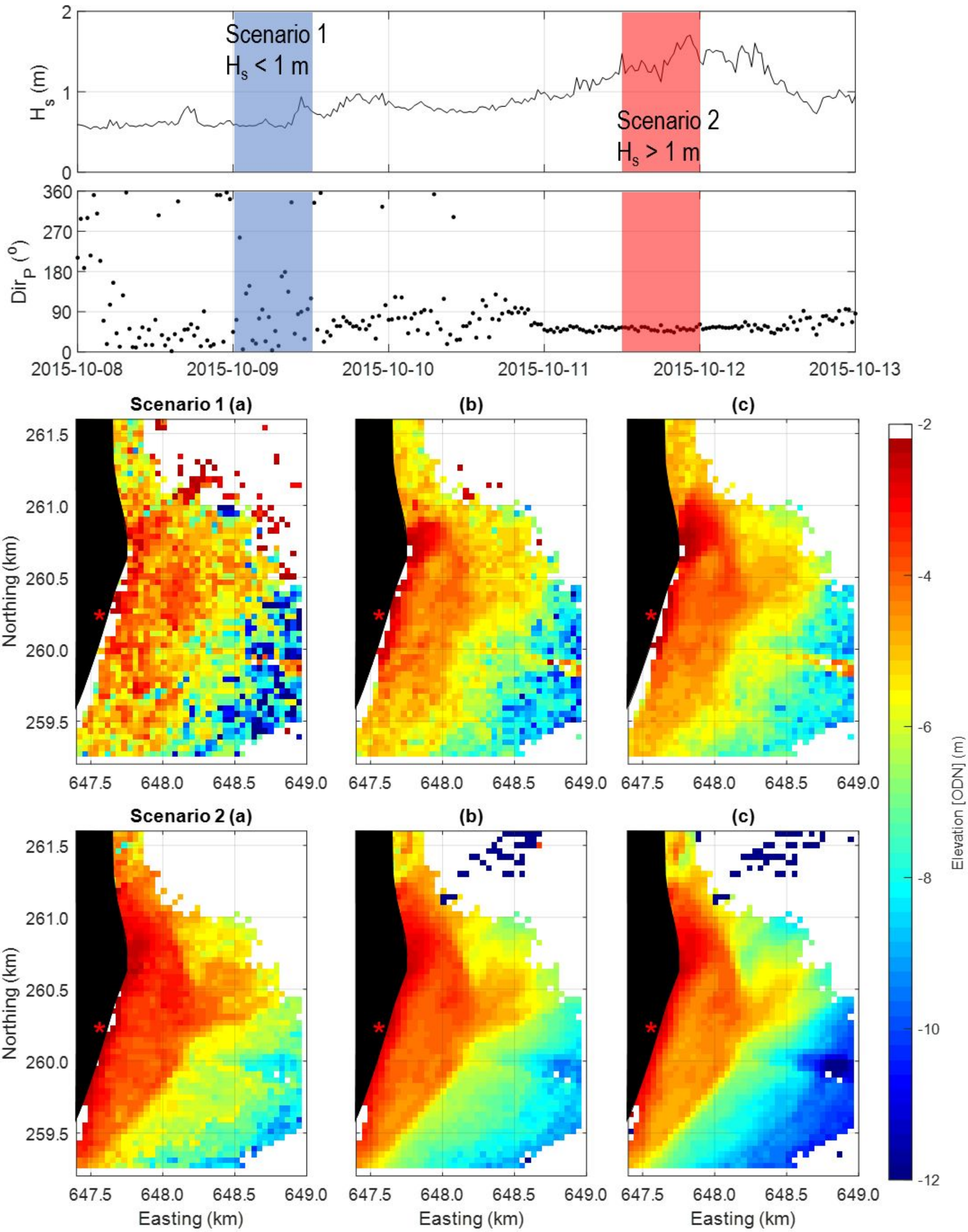

Scenario 1
H_s < 1 m
Scenario 2
H_s > 1 m
H_s (m)
Dir_P (^{o})
2015-10-08
2015-10-09
2015-10-10
2015-10-11
2015-10-12
2015-10-13
Scenario 1 (a)
(b)
(c)
Scenario 2 (a)
(b)
(c)
Northing (km)
Easting (km)
Elevation [ODN] (m)

Figure 5.

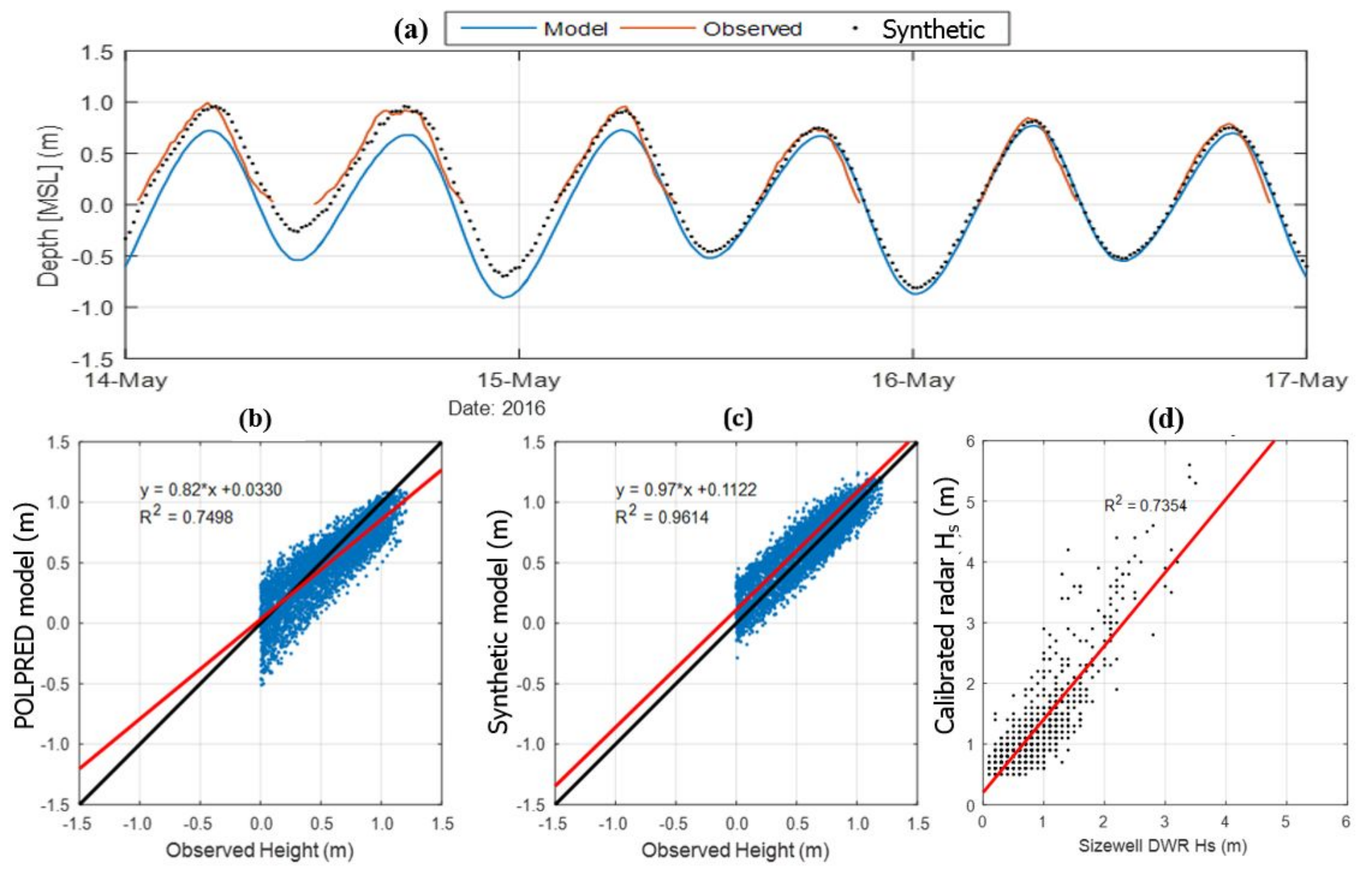

(a)
Model
Observed
Synthetic
Depth [MSL] (m)
1.5
1.0
0.5
0.0
-0.5
-1.0
-1.5
14-May
15-May
16-May
17-May
Date: 2016
(b)
y = 0.82*x +0.0330
R2 = 0.7498
POLPRED model (m)
Observed Height (m)
(c)
y = 0.97*x +0.1122
R2 = 0.9614
Synthetic model (m)
Observed Height (m)
(d)
R2 = 0.7354
Calibrated radar Hs (m)
Sizewell DWR Hs (m)

Figure 6.

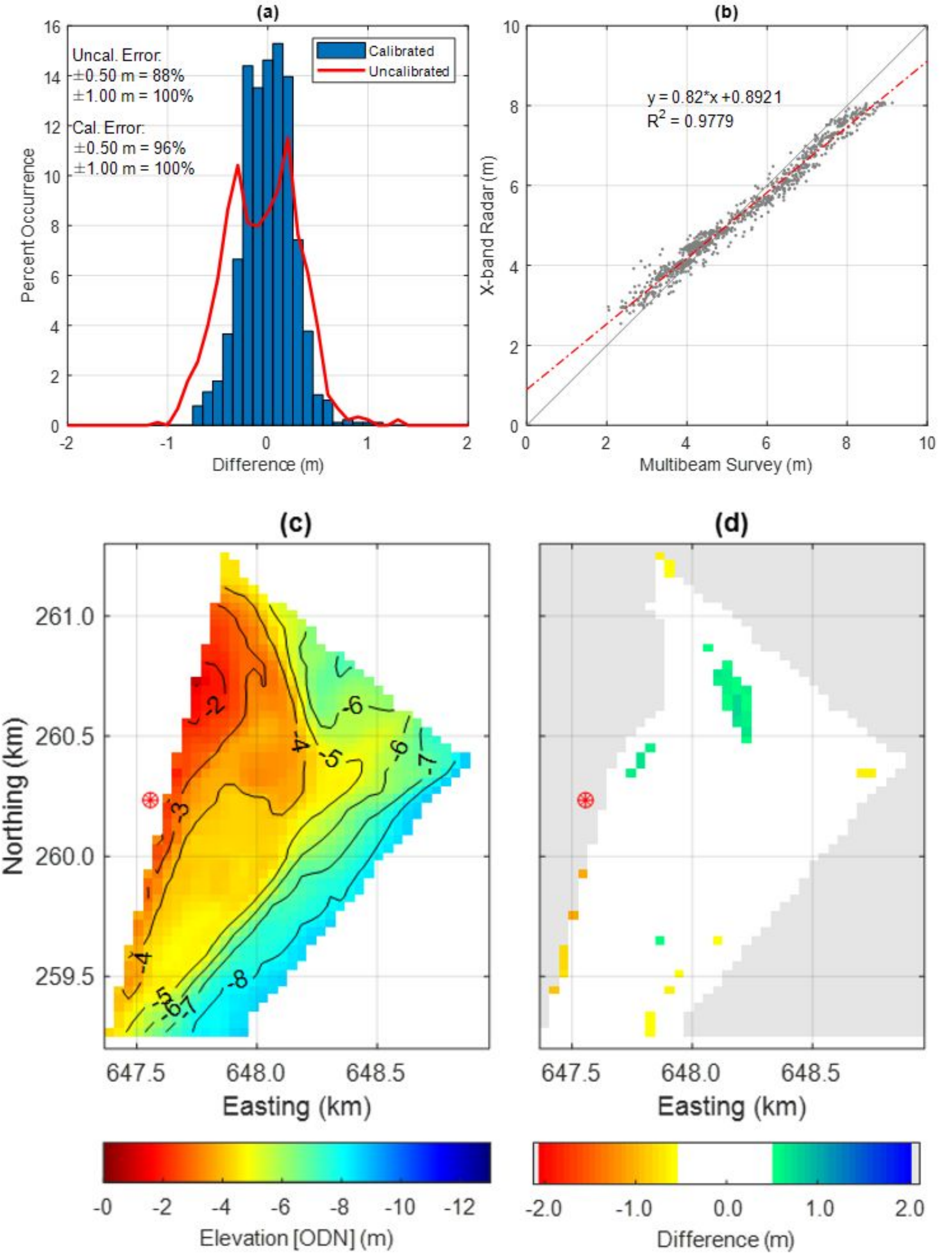
(a)
Uncal. Error:
±0.50 m = 88%
±1.00 m = 100%
Cal. Error:
±0.50 m = 96%
±1.00 m = 100%
Calibrated
Uncalibrated
Percent Occurrence
Difference (m)
(b)
y = 0.82*x +0.8921
R2 = 0.9779
X-band Radar (m)
Multibeam Survey (m)
(c)
Northing (km)
Easting (km)
Elevation [ODN] (m)
(d)
Easting (km)
Difference (m)

Figure 7.

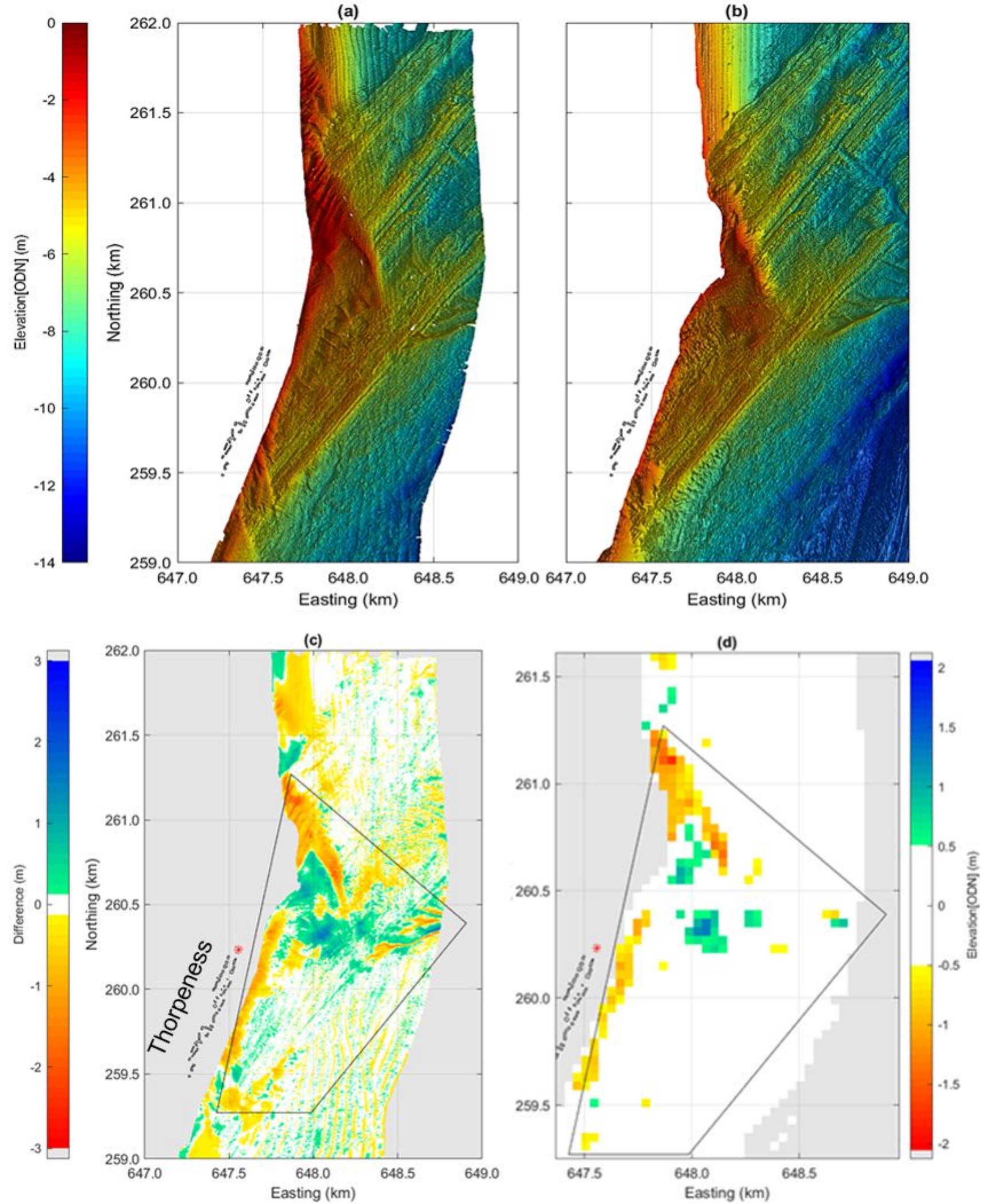
(a)
(b)
(c)
(d)
Elevation[ODN] (m)
Northing (km)
Easting (km)
Difference (m)
Thorpeness
Elevation[ODN] (m)

Figure 8.

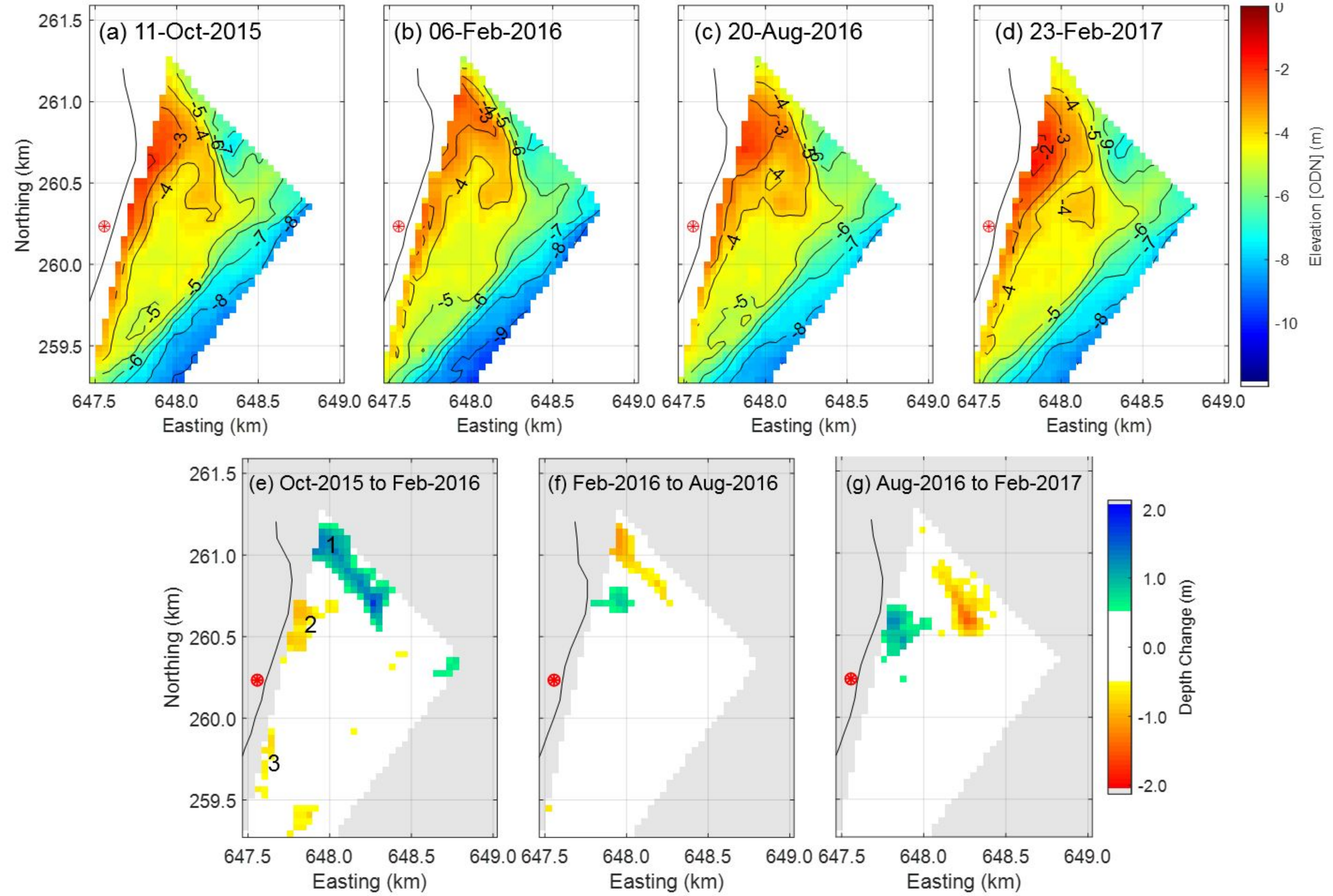

(a) 11-Oct-2015
(b) 06-Feb-2016
(c) 20-Aug-2016
(d) 23-Feb-2017
(e) Oct-2015 to Feb-2016
(f) Feb-2016 to Aug-2016
(g) Aug-2016 to Feb-2017
Northing (km)
Easting (km)
Elevation [ODN] (m)
Depth Change (m)
1
2
3

Figure 9.

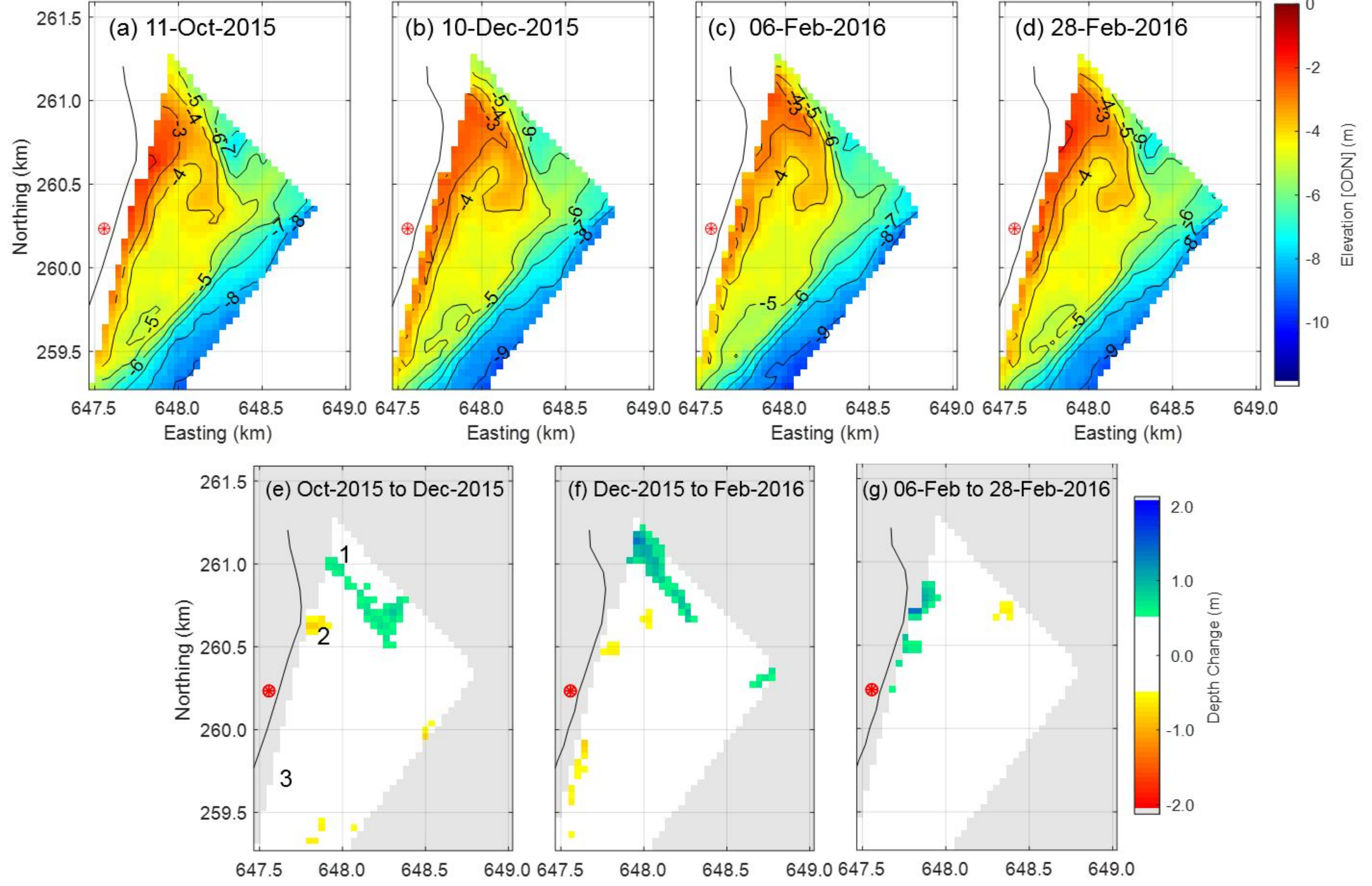

(a) 11-Oct-2015
(b) 10-Dec-2015
(c) 06-Feb-2016
(d) 28-Feb-2016
Northing (km)
Easting (km)
Elevation [ODN] (m)
(e) Oct-2015 to Dec-2015
(f) Dec-2015 to Feb-2016
(g) 06-Feb to 28-Feb-2016
Depth Change (m)